

# Optical Tomographic Brain Imaging with Diffusion and Transport Theory Based Algorithms

Andreas H. Hielscher<sup>\*a</sup>, Gassan S. Abdoulaev<sup>a</sup>,

Avraham Y. Bluestone<sup>a,b</sup>, Joseph Lasker<sup>a</sup>, Alexander Klose<sup>a</sup>

<sup>a</sup>Depts. of Biomedical Engineering & Radiology, Columbia University, New York, NY 10027

<sup>b</sup>Dept. of Pathology, State Univ. of New York - Downstate Medical Center, Brooklyn NY 11203

## ABSTRACT

There has been considerable discussion concerning the effects of the cerebrospinal fluid on measurements of blood-related parameters in the human brain, and if diffusion-theory-based image reconstruction algorithms can accurately account for the light propagation in the head. All of these studies have been performed either with synthetic data generated from numerical models or from phantom studies. We present here the first comparative study that involves clinical data from optical tomographic measurements. Data obtained from the human forehead during a Valsalva maneuver were input to two different model-based iterative image reconstruction algorithms recently developed in our laboratories. One code is based on the equation of radiative transfer, while the other algorithm uses a diffusion model to describe the light propagation in the head. Both codes use finite-element formulations of the respective theories and were used to obtain three-dimensional volumetric images of oxy, deoxy and total hemoglobin. The reconstructed overall spatial heterogeneity in changes of these parameters is similar using both algorithms. The two codes differ mostly in the amplitude of the observed changes. In general the transport based codes reconstructs changes 10-40% stronger than the diffusion code.

**Keywords:** Optical tomography, brain imaging, volumetric imaging, transport theory, diffusion approximation

## 1. INTRODUCTION

Several groups are currently pursuing the possibility of imaging the brain with diffuse optical tomography (DOT) [1-15]. Applications range from functional imaging [2-4,7,14] to the detection of hematomas [6,15]. For example, Benaron *et al* studied physiological changes in brain oxygenation in male adults during mixed motor and sensory cortex activation [1]. Hoshi *et al* [2] obtained quantitative images of hemoglobin concentration changes associated with neuronal activation in the human brain during a forward (DF) and backward (DB) digit span task, which assesses verbal working memory. Watanabe *et al.* have developed an optical system for obtaining 2-dimensional maps pinpointing the location of epileptic foci [3], and Franceschini *et al* have reported on imaging arterial pulsation and motor activation in healthy human subjects [4].

All clinical work in brain imaging and most tissue phantom studies use the diffusion theory and related equations in the analysis of the data. However, it is well known that the diffusion theory is only an approximation to the more widely applicable theory of radiative transfer [16,17]. While in many cases the diffusion theory is indeed a good approximation for describing light propagation in biological tissues, several researchers have theoretically and experimentally determined what the limits of this approximation are [18-24]. For example, it has been shown that the diffusion approximation fails when small sample geometries are considered in which source-detector separations are small and boundary effects are dominant. Furthermore, transport theory is more accurate when the medium contains regions in which the absorption coefficient is not much smaller than the scattering coefficient or when regions are considered in which the scattering and absorption are very low, so-called void-like regions. An example for void-like regions are the cerebrospinal-fluid-filled space in the brain. How these spaces affect light propagation has been the subject of many studies and discussions [20-24]. These studies, including our own work, have in general been limited to numerical examples, and a few studies involving measurements on tissue phantoms. An example is shown in Fig. 1, which shows results obtained with a 4x4cm tissue phantom that is made out of highly scattering resin ( $\mu_a = 0.35 \text{ cm}^{-1}$ ,

---

\* email: ahh2004@columbia.edu

$\mu_s' = 116 \text{ cm}^{-1}$ ) and contains a ring of water. Directing laser light onto one side of this sample we measured the transmitted light intensities at the adjacent side (y-axis) and the far-side (x-axis) of the sample, and compared the results with a diffusion-theory-based code and a transport code. The calculation were done on a  $241 \times 241$  x-y-grid with grid point x separations of  $\Delta x = \Delta y = 0.0167 \text{ cm}$ . For the diffusion code Robin boundary conditions were implemented, while in the transport code non-reentry boundary conditions were used. In both cases the difference of refractive index between the resin ( $n_r = 1.56$ ) and air ( $n = 1$ ) was considered. For the transport calculation an anisotropy factor of  $g = 0.8$  was assumed and the angular variable was discretized into 32 ordinates. To match the experimental condition to the two-dimensional simulation, a line source that extend  $\pm 5 \text{ cm}$  beyond the plane of measurement. (For more details concerning the transport code and the experimental setup see reference [25]). As Figs. 1b and 1c show the experimental results agree well with the numerical results obtained with the transport theory algorithm, while considerable difference between diffusion theory results and experiments exists.

In the here presented work we go beyond these phantom studies and show the first clinical reconstruction results that were generated with a model-based iterative image reconstruction (MOBIIR) code, which uses the equation of radiative transfer (ERT) as a model of light propagation in tissue. The results are compared to previously presented reconstructions that relied on a diffusion model.

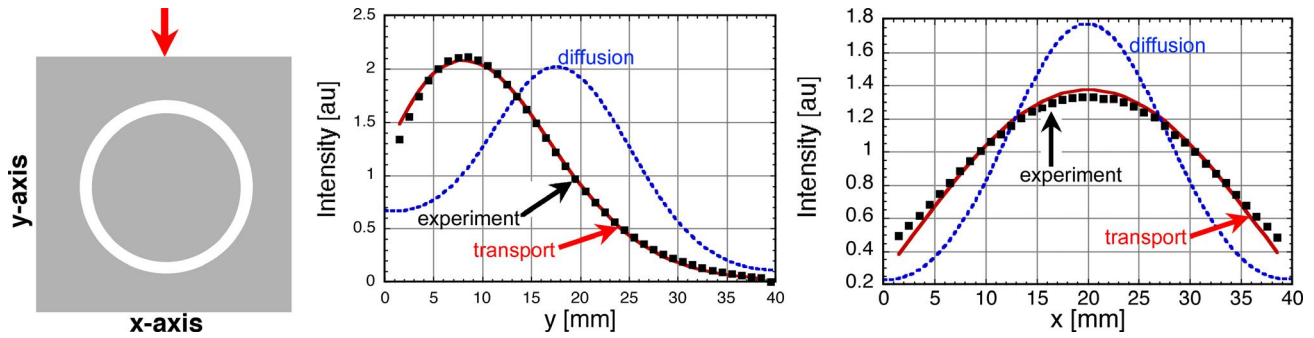


Fig 1. a,b,c. Experimental and numerical results for a highly scattering medium ( $\mu_s' = (1-g) \mu_s = 10 \text{ cm}^{-1}$ ,  $\mu_a = 0.1 \text{ cm}^{-1}$ ) that contains a low-scattering, water-filled ring. For an incident laser beam (red arrow left figure) the transmitted light intensities along the y-axis (middle) and x-axis (right) were measured. In addition, numerical calculations were performed with a 3D finite-difference algorithm that use either the diffusion equation or the equation of radiative transfer. Clearly visible are the good agreement between measurements and the transport model, whereas the diffusion model is less accurate.

## 2. METHODS

### 2.1. Image Reconstruction Algorithm

The 3-dimensional reconstruction of the optical properties in the human head is achieved using a model-based iterative image reconstruction (MOBIIR) scheme [26-29]. Our MOBIIR scheme comprises three major parts: (1) a forward model that predicts the detector readings based on a given spatial distribution of optical properties, (2) an objective function  $\Theta$  that compares predicted with measured signals, and (3) an updating scheme that uses the gradient of the objective function with respect to the optical properties to provide a means of updating the optical parameters for subsequent forward calculations.

As forward model we employ the time-independent equation of radiative transfer [30]

$$\omega \nabla \Psi(\mathbf{r}, \omega) + (\mu_a + \mu_s) \Psi(\mathbf{r}, \omega) = S(\mathbf{r}, \omega) + \mu_s \int_{4\pi} p(\omega, \omega') \Psi(\mathbf{r}, \omega') d\omega' \quad (1)$$

as well as the time-independent diffusion equation

$$\frac{\partial}{\partial x} \left( \partial \frac{\partial \Phi}{\partial x} \right) + \frac{\partial}{\partial y} \left( \partial \frac{\partial \Phi}{\partial y} \right) + \frac{\partial}{\partial z} \left( \partial \frac{\partial \Phi}{\partial z} \right) - c \mu_a = S \quad (2)$$

with

$$\Phi = \int_{4\pi} \Psi(\mathbf{r}, \omega) d\omega. \quad (3)$$

To bring the transport equation (1) into a suitable form for a finite-element scheme and to be able to apply an efficient adjoint differentiation algorithm for the inverse problem, we employ an even parity approach. This leads to a representation of Eq. 1 that allows to introduce a variational principle [31,32] and to use the finite element method to solve the problem numerically. For more details concerning this approach see reference [30]. The diffusion equation (2) is solved using a finite-element forward solver based on the Galerkin weak form of Eq. 1 [33-35]. This approach incorporates a Bramble-Pasciak XU (BPX) multi-grid preconditioner and an optimized conjugate gradient matrix solver. Furthermore we imposed Robin boundary conditions along all exterior surfaces.

The objective function that determines the goodness-of-fit between measured data,  $M$ , and predicted detector data,  $P$ , has been defined as

$$\Theta = \sum_s \sum_d \frac{\left[ \left( \frac{M_{sd}^{pert(t)}}{M_{sd}^{ref}} P_{sd}(\xi_0) \right) - P_{sd}(\xi_n) \right]^2}{\left[ \frac{M_{sd}^{pert(t)}}{M_{sd}^{ref}} P_{sd}(\xi_0) \right]^2} . \quad (4)$$

Here the relative changes  $(M_{sd}^{pert} / M_{sd}^{ref})$  are multiplied with the predicted detector readings  $P_{s,d}$  obtained from an initial distribution  $\xi_0 := (\mu_{a,0}, D_0)$  of the optical properties (typically assumed to be homogeneous). In subsequent iterations a distribution  $\xi := (\mu_a, D)$  is sought that produces the prediction  $P_{s,d}(\xi)$  that most closely matches  $(M_{sd}^{pert} / M_{sd}^{ref}) P_{s,d}(\xi_0)$ . The resulting distribution  $(\xi - \xi_0)$  is then a spatial representation of the differences in optical properties that led to the differences measured between  $M_{sd}^{pert}$  and  $M_{sd}^{ref}$ . Generally, one can look at the difference between rest  $M_{sd}^{ref}$  and corresponding time points  $M_{sd}^{pert(t)}$  during a perturbation, where  $s$  and  $d$  refer to sums over all sources and detectors, respectively.

This definition allows for the use of difference data. In a “difference” measurement approach one is unable to determine the absolute detector readings for a single time point and hence must compare the change in detector readings between two states; a pre and post perturbation state. This method has two main advantages: first, it is less sensitive to boundary effects and second; it is less sensitive to the initial guess chosen for the background medium [36]. Its major disadvantage is that one cannot determine the absolute distribution of optical properties, only the change in optical properties from a baseline. Many groups have used this approach, however, for localizing brain activity and for determining general trends in the oxygenation state [1,8,37].

The image reconstruction process is started with an initial guess of optical properties, in our case  $\xi_0 = (\mu_a = 0.1 \text{ cm}^{-1}, \mu_s' = 10 \text{ cm}^{-1})$ . Using this initial guess the detector readings  $P_{s,d}(\xi_0)$  are calculated with the finite element forward solver over the domain of interest, and the value of the objective function is determined. To update the initial distribution of optical properties, we calculate the gradient of the objective function with respect to all optical properties ( in the transport case  $[\partial\Theta / \partial\mu_a, \partial\Theta / \partial\mu_s]$ ; in the diffusion case  $[\partial\Theta / \partial\mu_a, \partial\Theta / \partial D]$ ). This gradient defines a “direction” of minimum descent, which is then used in a multidimensional conjugate gradient descent algorithm that minimizes the objective function [26,27,35].

The calculation of the gradient was performed using the technique of adjoint differentiation [26-28, 35, 38, and 39]. In this case, the computational burden for the gradient calculation is on the order of one forward calculation. The objective function and gradient algorithm is incorporated in a multidimensional conjugate gradient descent algorithm where typically 15-30 iterations with different gradients are necessary before convergence is achieved.

## 2.2. Determination of surface coordinates and mesh generation

For model-based optical tomographic imaging reconstructions one has to determine the surface geometry and source-detector locations. To achieve this we employed the techniques of photogrammetry [40-42]. To determine the 3-dimensional coordinates of the surface of the forehead as well as all source-detector locations we placed circular reflective markers on the head. These markers have the advantage of allowing sub-pixel precision when used in combination with the centroid-locating algorithm. Once all markers were placed on the surface of the head, the area of

interest was photographed from different angles with a digital camera (SONY Mavika FD-90). These images of the head were then transferred to a desktop computer for analysis with the commercially available Photogrammetry software package (Photomodeler, Eos Systems Inc., Vancouver, Canada). After the targets in the photographs were marked and referenced we processed the images using the “bundle adjustment algorithm,” which computed all 3D coordinates of all referenced points.

Having generated the surface coordinates of the human head, the boundary of our domain, it was necessary to build the corresponding volume. To this end, the coordinates of the surface points obtained using the photogrammetric approach were exported to a volumetric mesh generator. For this procedure, we used the CAD style volume generator GID software package (GID, CIMNE Inter. Center for Num. Methods, Barcelona, Spain). This package allowed us to manually extend the surface in the z direction by 4.0 cm and build the corresponding volume mesh, which are required for the reconstruction. Since computational time depends on the number of mesh nodes, we limited the volume to a 4.0 cm zone beneath the surface of interest, and not to the entire head. We found that larger volumes are not necessary to consider, since their influence on the reconstruction results is negligible. The final mesh used for the forehead calculations consisted out of 11255 nodes, resulting in an average distance between nodes of  $\sim 0.2$ cm. More details on the photogrammetry approach and the mesh generation can be found in reference [43].

### 2.3. Instrumentation and data acquisition

Measurements on the human forehead are performed with the dynamic near-infrared optical tomography instrument, recently developed by Schmitz *et al* [44,45]. This instrument operates in continuous-wave mode. Beams from two laser diodes with wavelength of  $\lambda_1 = 760$  nm and  $\lambda_2 = 830$  nm are coupled into a set of source fiber bundles. The laser diodes are modulated at 5KHz and 7KHz, respectively. The demodulated signal allows for the simultaneous measurement of the intensity at all detectors for a given source position at both wavelengths. Having this dual-wavelength capability allows for the elucidation of both oxyhemoglobin and deoxyhemoglobin. For the measurements presented in this work we used 4 sources and 15 detectors, resulting in 60 source-detector combinations. Figure 2 shows the locations of the sources and detectors on the forehead. A three-tiered band was used to secure 3 sets of 5 optodes per tier to the left forehead. Each optode consisted of a co-located source and detector, and all measurements were performed simultaneously at the two wavelengths. Three tomographic data sets, involving all 60 source-detector pairs, were acquired per second.

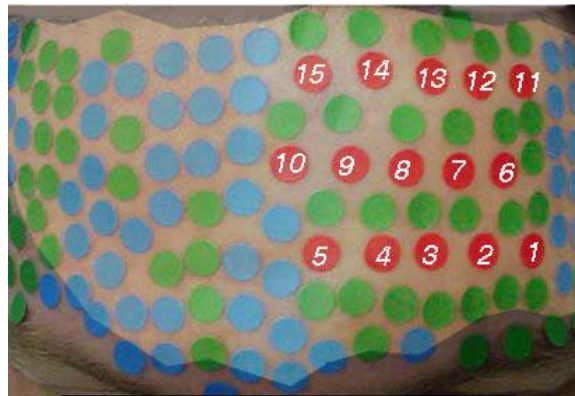


Fig. 2: Placement of sources and detectors on forehead. The 15 source/detector position are indicated by the encircled numbers. Other round dots indicate reference points used for the photogrammetric surface determination. The lighter shaded area depicts the outer surface of the finite-element mesh, which was used for the volumetric image reconstruction (see Figs. 4-6).

### 2.4. Experimental Protocol

The experiment was designed to look at functional hemodynamic changes in the forehead of a single patient induced by a Valsalva maneuver. For the measurement the patient was placed in the supine position. Three epochs consisting of Valsalva maneuvers with one-minute rest periods interspersed were performed. During the Valsalva maneuver a forced expiration against a closed glottis demonstrates the effects of changes in intrathoracic pressure on blood pressure, and the brain’s autoregulatory response to decreased vascular perfusion pressure in cerebral vessels [46].

Assuming that the primary influences on the changes in the absorption coefficients at each wavelength are a linear combination of oxyhemoglobin and deoxyhemoglobin, one arrives at two equations for oxyhemoglobin, (HbO<sub>2</sub>), and deoxyhemoglobin (Hb) concentration changes [47,48]:

$$\Delta[Hb]_{meas} = \frac{\epsilon_{HbO}^{\lambda_2} \Delta\mu_a^{\lambda_1} - \epsilon_{HbO}^{\lambda_1} \Delta\mu_a^{\lambda_2}}{\epsilon_{Hb}^{\lambda_1} \epsilon_{HbO}^{\lambda_2} - \epsilon_{Hb}^{\lambda_2} \epsilon_{HbO}^{\lambda_1}}, \quad (5)$$

$$\Delta[HbO_2]_{meas} = \frac{\epsilon_{Hb}^{\lambda_2} \Delta\mu_a^{\lambda_1} - \epsilon_{Hb}^{\lambda_1} \Delta\mu_a^{\lambda_2}}{\epsilon_{Hb}^{\lambda_1} \epsilon_{HbO}^{\lambda_2} - \epsilon_{Hb}^{\lambda_2} \epsilon_{HbO}^{\lambda_1}}. \quad (6)$$

The parameters  $\epsilon_{Hb}$  and  $\epsilon_{HbO}$  are the known extinction coefficients for deoxyhemoglobin and oxyhemoglobin at the given wavelengths [48], respectively. The  $\Delta\mu_a$ 's are the calculated changes in the absorption coefficients at each node of the mesh determined using the MOBIIR reconstruction algorithm.

### 3. RESULTS

A trace of the measured output produced by the optical image system is shown in Fig. 2. Displayed are fifteen traces of the normalized (to the rest period) and smoothed (length 5 median filter) measured intensity profiles during one Valsalva maneuver for source position three at a wavelength of 760nm. At  $t = 10$  seconds the Valsalva maneuver began. After a small initial dip an increase in signal was observed, which returned to baseline within 25-35 seconds. Then the signal decreased steadily and approached a minimum at  $t = 95$  seconds, at which point the subject started to breath normally again. The signal rapidly recovered and returned to base line.

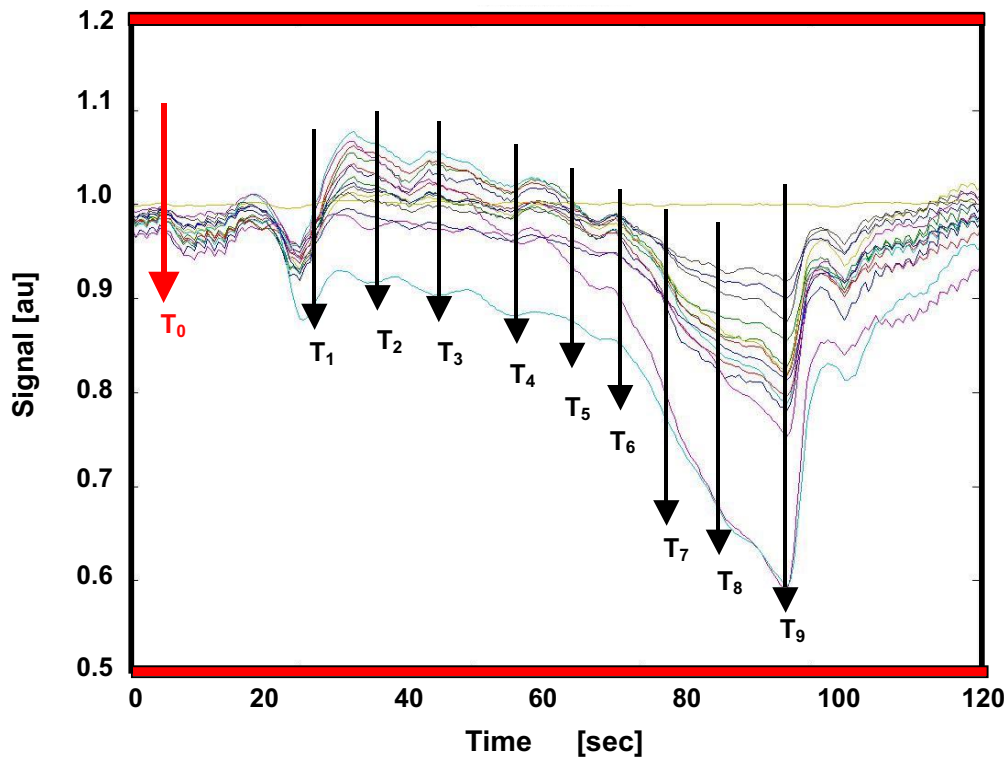
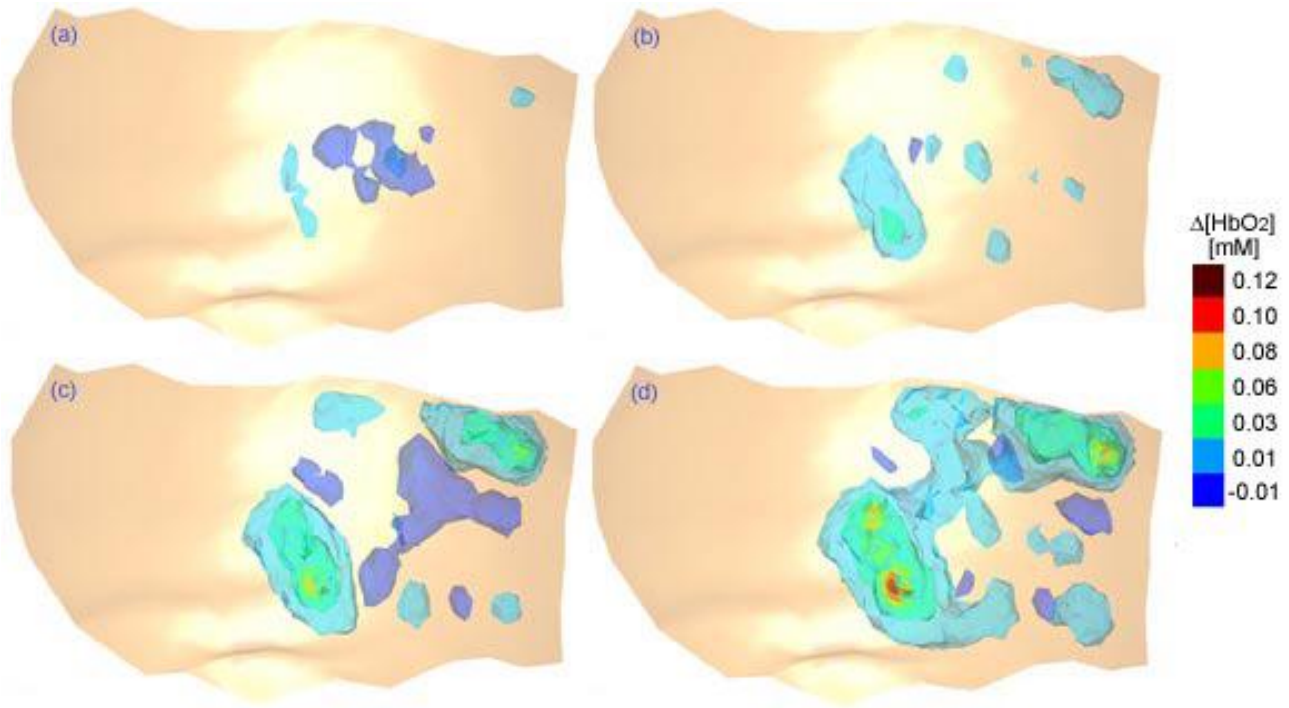
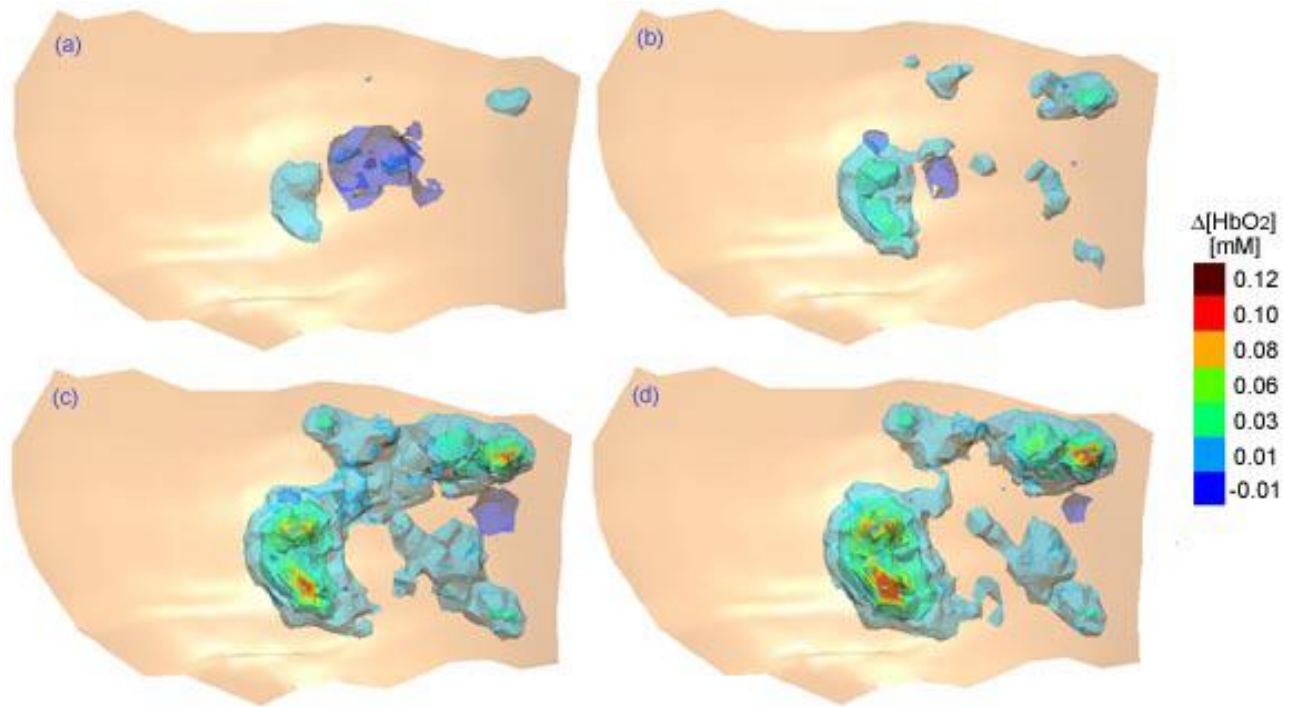


Fig. 3. Median-filtered time series for a Valsalva maneuver epoch.



**Fig. 4.** Diffusion-theory-based reconstructed of changes in deoxyhemoglobin at time points T2 (a), T5 (b), T8(c) and T9 (d) (see Fig. 3) during a Valsalva maneuver. Shown are frontal views of the forehead as seen in Fig. 1. The calculations were performed on a finite-element mesh with 11255 nodes, resulting in an average distance between nodes of  $\sim 0.2\text{cm}$ .



**Fig. 5.** Transport-theory-based reconstructed of changes in deoxyhemoglobin at time points T2 (a), T5 (b), T8(c) and T9 (d) (see Fig. 3) during a Valsalva maneuver. Shown are frontal views of the forehead as seen in Fig. 2. The calculations were performed on a finite-element mesh with 11255 nodes, resulting in an average distance between nodes of  $\sim 0.2\text{cm}$ .

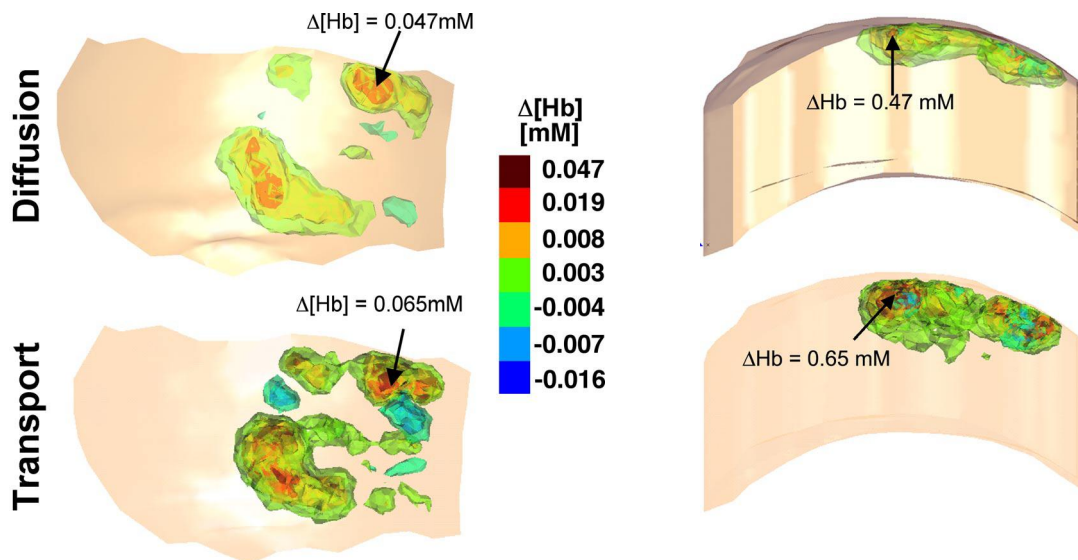


**Fig. 6:** Comparison of diffusion and transport based reconstruction results at time  $T_9$  (see Fig.3). The top row shows diffusion-theory-based results calculated from data obtained from the forehead of a human subject during a Valsalva experiment. Displayed are head-on view on the left and aerial view (from the top of the head) on the right. The bottom row shows the same views, however, the image reconstruction was based on the equation of radiative transfer. The calculations were performed on a finite-element mesh with 11255 nodes, resulting in an average distance between nodes of  $\sim 0.2$ cm.

For the “difference” reconstruction we used the ratio of the data at the time points indicated by the black arrows, with respect to data at time point  $t = T_0$  (Fig. 3). Figures 4-6 show the three-dimensional distribution of the reconstructed values for changes in deoxyhemoglobin (Hb) and oxyhemoglobin ( $HbO_2$ ) at selected time points. The different colors (shadings) represent isosurfaces of constant oxyhemoglobin and deoxyhemoglobin concentration changes relative to the reference point at  $T_0$ . All diffusion reconstructions were stopped after 25 iterations. At that time no further changes in the reconstructed distributions were observed. The time for a reconstruction of an oxy or deoxyhemoglobin image using the diffusion code was approximately 4 hours on a Pentium III 550Mhz processor. This time includes the reconstruction of the absorption changes at two wavelengths for a mesh with 11255 nodes. The transport-theory based code converged after 12 iterations, which took approximately 16 hours on the same workstation. The difference in the number of iterations required for convergence, most likely results from different optimization schemes used in the diffusion and transport algorithms. While the diffusion-based code employs a conjugate-gradient method, which requires complete line minimization, the transport code used a BFGS minimization method [49], which does not require complete line searches.

In Figs. 4 and 5 front views of changes in oxyhemoglobin distribution in the forehead are shown for 4 different time points ( $T_2$ ,  $T_5$ ,  $T_8$ , and  $T_9$ ). Figure 4 shows the reconstruction results based on the diffusion model, while Fig. 5 shows the results obtained with the transport-theory-based code. Changes are only visible in the area of measurements on the right side of the forehead. No optical probes were placed on the left side of the head (see Fig. 2). One observes that the overall time evolution of changes and the distribution at any given time point are similar. Yet, the two reconstruction scheme also produce notable differences. For example, at timepoint  $T_8$  (Figs. 4c and 5c), the diffusion code reconstruct a decrease in  $[HbO_2]$  for a large triangular regions in the center of the right forehead, while the transport code shows a small increase. Furthermore, we noted that the value of the maximal changes can differ substantially. For example, the maximal change at time point  $T_9$  is 0.15mM if a diffusion code is used, but almost 50% higher (0.22mM) when a transport code is employed.

Similar results are found when changes in deoxyhemoglobin are reconstructed. Figure 6 shows an example for data obtained at time-point  $T_9$ . While one observes similarities in the overall spatial distribution, the values of the maximal changes in deoxyhemoglobin concentration differ markedly. The diffusion code finds maximal changes in  $[Hb]$  of 0.047mM, while the transport code finds 0.065mM. Also the center of this change is slightly shifter to larger depth, which can be see most clearly in the aerial view. The transport results locate the maximal change approximately 0.5 cm deeper inside the head than the diffusion analysis.

That no larger differences are observed may have several reasons. First it should be noted that only changes in optical and physiological properties were reconstructed. Pei *et al* [36] have recently shown that in this case the forward model does not play such an important role. Hillman *et al* [50], however, have reported in another study that even for relative data the accuracy of the forward model cannot be neglected. Another reason for the small difference could be the fact that the transport code was used with an isotropic scattering phase function, instead of an anisotropic scattering phase function. Anisotropic scattering phase function require a fine angular discretization, which leads to increased memory requirements and computation times. Furthermore, the spatial discretization of  $\sim 0.2\text{cm}$  between adjacent nodes may not be small enough to capture all effects. Finally, the expected effect of the cerebrospinal-fluid layer may be smaller than expected. Additional studies will be necessary to explore all these aspects and to determine in what cases the diffusion approximation suffices and when a transport-theory-based algorithm is required.

#### 4. SUMMARY

We presented the first study that compares diffusion-theory-based and transport-theory-based image reconstruction codes using clinical data from optical tomographic measurements. Data were obtained from the human forehead during a Valsalva maneuver. The data were input to two different model-based iterative image reconstruction algorithms recently developed in our laboratories. The algorithms were used to obtain three-dimensional volumetric images of oxy- and deoxy-hemoglobin. The reconstructed overall spatial heterogeneity in changes of these parameters is similar for both algorithms. The two codes differ mostly in the amplitude of the observed changes. In general the transport based codes reconstructs changes 10-40% stronger than the diffusion code. Furthermore, using a transport-theory-based algorithm, the changes appeared to be located deeper inside the head. That the observed differences between diffusion-theory-based and transport-theory based reconstruction were not as large as expected may be due to the fact that relative measurements and reconstruction were performed. Other factors, such as level of spatial and angular discretization or the geometry of the subarachnoid space and unknown optical properties of certain parts of the brain, may also be responsible for the observed similarities. More work is necessary to fully resolve these issues.

#### ACKNOWLEDGMENTS

This work was supported in part by the New York City Council Speaker's Fund for Biomedical Research: Toward the Science of Patient Care, and an SBIR grant from the National Heart, Lung, and Blood Institute (NHLBI) (grant # 2R44-HL-61057-02), which is part of the National Institutes of Health.

#### REFERENCES

1. D. A. Benaron, S. R. Hintz, A. Villringer, D. Boas, A. Kleinschmidt, J. Frahm, C. Hirth, H. Obrig, J. C. Van Houten, E. L. Kermit, W. Cheong, D. K. Stevenson, "Noninvasive functional imaging of human brain using light," *J. Cerebral Blood Flow and Metabolism* **20**, 469-477 (2000).
2. Y. Hoshi, I. Oda, Y. Wada, Y. Ito, Y. Yamashita, M. Oda, K. Ohta, Y. Yamada, M. Tamura, "Visuospatial imagery is a fruitful strategy for the digit span backward task: a study with near-infrared optical tomography," *Cognitive Brain Research* **9**, 339-342 (2000).
3. E. Watanabe, A. Maki, F. Kawaguchi, Y. Yamashita, H. Koizumi, Y. Mayanagi, "Noninvasive cerebral blood volume measurement during seizures using multichannel near infrared spectroscopic topography," *J. Biomed. Opt.* **5**, 287-290 (2000).
4. M. Franceschini, V. Toronov, M. E. Filiaci, E. Gratton, S. Fantini, "On-line optical imaging of the human brain with 160-ms temporal resolution," *Optics Express* **6**, 49-57 (2000).
5. S. Fantini, D. Huebert, M. A. Franceschini, E. Gratton, W. Rosenfeld, P. G. Stubblefield, D. Maulik, and M. Stankovic, "Non-invasive optical monitoring of the newborn piglet brain using continuous-wave and frequency-domain spectroscopy," *Phys. Med. Biol.* **44**, 1543-1563 (1999).

6. M. R. Stankovic, D. Maulik, W. Rosenfeld, P. G. Stubblefield, A. D. Kofinas, S. Drexler, R. Nair, M. A. Franceschini, D. Hueber, E. Gratton, and S. Fantini, "Real-time optical imaging of experimental brain ischemia and hemorrhage in neonatal piglets", *J. Perinat. Med.* **27**, 279-286 (1999).
7. H. Koizumi, Y. Yamashita, A. Maki, T. Yamamoto, Y. Ito, H. Itagaki, and R. Kennan, "Higher-Order Brain Function Analysis by trans-cranial dynamic near-infrared spectroscopy imaging," *J. Biomed. Opt.* **4**, 403-413 (1999).
8. A. Villringer and B. Chance, "Non-invasive optical spectroscopy and imaging of human brain function," *Trends Neuroscience* **20**, 435-442 (1997).
9. M. Tamura, Y. Hoshi, and F. Okada, "Localized near-infrared spectroscopy and functional optical imaging of brain activity," *Philosophical Transactions of the Royal Society of London - Series B: Biological Sciences* **352**(1354), 737-42, (1997).
10. A. Kleinschmidt, Hellmuth Obrig, M. Requardt, K. Merboldt, U. Dirnagl, A. Villringer, and J. Frahm, "Simultaneous recording of cerebral blood oxygenation changes during human brain activation by magnetic resonance imaging and near infrared spectroscopy", *J. Cerebral Blood Flow and Metabolism* **16**, 817-826 (1996).
11. H. Liu, B. Chance, A. H. Hielscher, S. L. Jacques, F. K. Tittel, "Influence of blood vessels on the measurement of hemoglobin oxygenation as determined by time-resolved reflectance spectroscopy," *Med. Phys.* **22**, 1209-1217 (1995).
12. G. Gratton and M. Fabiani, "Dynamic brain imaging: Event-related optical signal (EROS) measures of the time course and localization of cognitive-related activity," *Psychonomic Bulletin and Review* **5**, 535-563, (1995).
13. A. Maki, Y. Yamashita, Y. Ito, E. Watanabe, Y. Mayanagi, H. Koizumi, "Spatial and temporal analysis of human motor activity using non-invasive NIR topography," *J. Med. Phys.* **22**, 1997-2005 (1995).
14. Y. Hoshi and M. Tamura, "Detection of dynamic changes in cerebral oxygenation coupled to neuronal function during mental work in man," *Neuroscience Letters* **150**, 5-8 (1993).
15. Hintz S.R., W.F. Cheong, J.P. van Houten, D.K. Stevenson, D.A. Benaron, "Bedside imaging of intracranial hemorrhage in the neonate using light: comparison with ultrasound, computed tomography, and magnetic resonance imaging", *Pediatr. Res.* **45**, 54-59 (1999).
16. Ishimaru A, "Diffusion of light in turbid material," *Applied Optics* **28**(12), pp. 2210-2215 (1989).
17. Ishimaru A, *Wave propagation and scattering in random media*, Academic, New York, 1978.
18. Hielscher AH, Alcouffe RE, Barbour RL, "Comparison of finite-difference transport and diffusion calculations for photon migration in homogeneous and heterogeneous tissue," *Phys Med Biol* **43**, pp. 1285-1302 (1998).
19. Dehghani H, Delpy DT, Arridge, SR, "Photon migration in non-scattering tissue and the effects on image reconstruction," *Physics in Medicine and Biology* **44**(12), pp.2897-2906 (1999).
20. Ripoll J, Nieto-Vesperinas M, Arridge, SR, Dehghani H, "Boundary conditions for light propagation in diffusive media with nonscattering regions," *J Optical Society of America A* **17**(9), pp. 1671-1682 (2000).
21. Arridge SR, Dehghani H, Schweiger M, Okada E, "The finite element model for the propagation of light in scattering media: A direct method for domains with nonscattering regions," *Medical Physics* **27**(1), pp. 252-265 (2000).
22. Firbank M, Arridge SR, Schweiger M, Delpy DT, "An investigation of light transport through scattering bodies with non-scattering regions," *Physics in Medicine and Biology* **41**(4), pp. 767- (1996).
23. Okada E, Firbank M, Schweiger M, Arridge SR, Cope M, Delpy DT, "Theoretical and experimental investigation of near-infrared light propagation in a model of the adult head," *Applied Optics* **36**(1), pp. 21-32 (1997).
24. M. Schweiger, S.R. Arridge, "Optical tomographic reconstruction in a complex head model using a priori region boundary information," *Physics in Medicine and Biology* **44**(11), pp. 2703- (1999).
25. A.D. Klose, U. Netz, J. Beuthan, A.H. Hielscher, "Optical tomography using the time-independent equation of radiative transfer. Part 1: Forward model," *Journal of Quantitative Spectroscopy and Radiative Transfer*, Vol **72/5**, pp 691-713, 2002.
26. A.D. Klose, A.H. Hielscher, "Optical tomography using the time-independent equation of radiative transfer. Part 2: Inverse model," *Journal of Quantitative Spectroscopy and Radiative Transfer*, Vol **72/5**, pp 715-732, 2002.
27. A.D. Klose, and A.H. Hielscher, "Iterative reconstruction scheme for optical tomography based on the equation of radiative transfer," *Med. Phys.* **26**, 1698-1707 (1999).
28. A.H. Hielscher, A. D. Klose, K. M. Hanson, "Gradient-based iterative image reconstruction scheme for time-resolved optical tomography", *IEEE Trans Med Imag.* **18**, 262-271 (1999).
29. R. Roy and E. M. Sevick-Muraca, "Truncated Newton's optimization scheme for absorption and fluorescence optical tomography: Part I Theory and formulation," *Optics Express* **4**, 353-371 (1999).

30. G. Abdoulaev and A.H. Hielscher, "Three-dimensional optical tomography with the equation of radiative transfer," *Journal of Electronic Imaging* (in press)
31. S.Kaplan and J.A.Davis, "Canonical and Involutory Transformations of the Variational Problems of Transport Theory," *Nucl Sci Eng* **28**, pp. 166-176(1967).
32. C.R.E.deOliveira, "An Arbitrary Geometry Finite Element Method for Multigroup Neutron Transport with Anisotropic Scattering," *Progress in Nuclear Energy* **18**, pp. 227-236 (1986).
33. G. Abdoulaev, A. Varone and G. Zanetti, "An object oriented flow solver for the CRS4 virtual vascular project", in *Proceedings of the 3rd European conference on Numerical mathematics and advanced applications*, World Scientific, Singapore, pp. 407-415, 2000.
34. J. H. Bramble, J. E. Pasciak, and J. Xu, "Parallel multilevel preconditioners", *Math. Comp.* **55**, pp. 1-22, 1990.
35. A.Y. Bluestone, G. Abdoulaev, C. Schmitz, R.L. Barbour, A.H. Hielscher, "Three-dimensional optical-tomography of hemodynamics in the human head", *Optics Express* **9**(6), pp. 272-286, 2001. (<http://www.opticsexpress.org/abstract.cfm?URI=OPEX-9-6-272>)
36. Y. Pei Y, H.L. Graber, R.L. Barbour, "Influence of systematic errors in reference states on image quality and on stability of derived information for dc optical imaging," *Applied Optics* **40**(31), pp. 5755-5769 (2001).
37. D.A. Boas, T. Gaudette, G. Strangman, X. Cheng, J.J. Marota, J.B. Mandeville, "The accuracy of near infrared spectroscopy and imaging during focal changes in cerebral hemodynamics," *Neuroimage* **13**, 76-90 (2001).
38. A. J. Davies, D. B. Christianson, L. C. W. Dixon, R. Roy, and P. van der Zee, "Reverse differentiation and the inverse diffusion problem," *Advances in Engineering Software* **28**, 217-221 (1997).
39. D.B. Christianson , A. J. Davies, L. C. W. Dixon, R. Roy, P. Van der zee, "Giving Reverse Differentiation a Helping Hand," *Optimization Methods and Software* **8**, 53-67 (1997).
40. H. M. Karara, *Handbook of Non-topographic Photogrammetry* (American Society of Photogrammetry, Falls Church, VA, 1989).
41. E. F. Church, *Elements of Photogrammetry* (Syracuse University Press, New York, 1948).
42. G. Deng, W. Falg, "An evaluation of an off-the-shelf digital close-range photogrammetric software package," *Photogrammetric Engineering and Remote Sensing* **67**, 227-233 (2001).
43. A. Bluestone, G. Abdoulaev, R.L. Barbour, C.H. Schmitz, A.H. Hielscher, "Three-dimensional optical-tomographic localization of changes in absorption coefficients in the human brain," in *Optical Tomography and Spectroscopy of Tissue IV*, SPIE-Proceedings 4250, Bellingham, WA, 258-268 (2001).
44. C.H. Schmitz, M. Löcker, J.M. Lasker, A.H. Hielscher, R.L. Barbour, "Instrumentation for fast functional optical tomography," *Review of Scientific Instrumentation* **73**(2), pp. 429-439, 2002.
45. C.H. Schmitz, H.L.Grabr, H. Luo, I. Arif, J. Ira, Y. Pei, A. Bluestone, S. Zhong, R. Andronica, I. Soller, N. Ramirez, S.L.S. Barbour, and R.L. Barbour, "Instrumentation and calibration protocol for imaging dynamic features in dense scattering media by optical tomography," *Appl. Opt.* **39**, 6466-6485 (2000).
46. F. P. Tiecks, C. Douville, S. Byrd, A. M. Lam, D. W. Newell, "Evaluation of impaired cerebral autoregulation by the Valsalva Maneuver", *Stroke* **27**, 1177-1182 (1996).
47. X. Cheng, D.A.Boas, "Systematic diffuse optical image errors resulting from uncertainty in the background optical properties," *Optics Express* **4**, 299-307 (1999).
48. S. Wray, M. Cope, D.T. Delpy, "Characteristics of the near infrared absorption spectra of cytochrome aa<sub>3</sub> and hemoglobin for the noninvasive monitoring of cerebral oxygenation," *Biochim Biophys Acta* **933**, 184-192 (1988).
49. A.K. Klose, A.H. Hielscher, " Quasi-Newton methods in optical tomographic imaging," *Inverse Problems*, in press.
50. Hillman EMC, Dehghani H, Hebden JC, Arridge SR, Schweiger M, Delpy DT, "Differential imaging in heterogeneous media: limitations of linearization assumptions in optical tomography," in *Optical Tomography and Spectroscopy of Tissue IV*, B. Chance, R.R. Alfano, B.J. Tromberg, M. Tamura, E.M. Sevick-Muraca, eds., Proc. SPIE Vol. 4250, pp. 327-338 (2001).